CrossMark

An approach for estimating the largest probable tsunami from far-field subduction zone earthquakes

Nikos Kalligeris[1] · Luis Montoya[1] · Aykut Ayca[1] ·
Patrick Lynett[1]

Abstract Following the recent unexpected earthquake events of 2004 and 2011, it can be cautiously extrapolated that all major subduction zones bearing the capacity to produce mega-earthquake events will eventually do so given enough time, irrespective of the lack of such in the relatively short historical record. This notion has led to an effort of assigning maximum earthquake magnitudes to all major subduction zones, either based on geological constraints or based on size–frequency relations, or a combination of both. In this study, we utilize the proposed maximum magnitudes to assess tsunami hazard in Central California in the very long return periods. We also assessed tsunami hazard following an alternative methodology to calculate maximum magnitudes, which uses scaling relations for subduction zone earthquakes and maximum fault rupture scenarios found in literature. A sensitivity analysis is performed for Central California that is applicable to any coastal site in the Pacific Rim and can readily provide a strong indication for which subduction zones beam the most energy toward a study area. The maximum earthquake scenarios are then narrowed down to a few candidates, for which the initial conditions are examined in more detail. The chosen worst-case scenarios for Central California stem from the Alaska–Aleutian subduction zone that beams more energy and generates the biggest amplitude waves toward the study area. The largest tsunami scenario produces maximum free surface elevations of 15 m and run-up heights greater than 20 m.

Keywords Tsunami · Hazard · Numerical modeling · Worst-case scenario · Maximum magnitude earthquake · Far field

✉ Luis Montoya
   lhmontoy@usc.edu

[1] Department of Civil and Environmental Engineering, University of Southern California,
   Los Angeles, CA 90089, USA

1 Introduction

In the aftermath of the 2004 Sumatra–Andaman and 2011 Tohoku earthquakes, the capability of subduction zones (SZ) to generate mega earthquakes is being re-visited (Geller 2011; Kagan and Jackson 2013). This has a direct consequence on Tsunami Hazard Assessment (THA) studies for sensitive infrastructure for which long return period events control the hazard. The Fukushima Nuclear Power Plant disaster (Synolakis and Kanoglu 2015), an aftereffect of the Tohoku earthquake and ensuing tsunami, raised global safety concerns on nuclear power plants and revealed weaknesses on the non-standardized methodology involved in THA studies. This disaster was a lesson learned in the tsunami community's quest for wisdom, through which significant progress has been made throughout the years on all fronts, namely in terms of science, warning and mitigation (Okal 2015).

The State of California has been following the gradual leap in knowledge and technology to periodically re-assess tsunami hazard and risk on its coastline in light of new findings. Houston and Garcia (1978) were the first to perform a probabilistic THA and establish the 100- and 500-year tsunami run-up elevations on the US west coast using a threshold model. Synolakis et al. (1997) proposed a new methodology to estimate tsunami risk in California using a state-of-the-art numerical model that allows for on-land run-up/inundation computations. Drawing knowledge from the findings of the 1998 Papua Guinea field survey (Synolakis et al. 2002), there was more emphasis on submarine landslide-generated tsunamis, which were not widely considered in THA studies. Borrero et al. (2001) were the first to present hydrodynamic simulations of landslide tsunamis in Southern California. Eisner et al. (2001) and Barberopoulou et al. (2009) developed inundation maps for the State of California, while Lynett et al. (2014) and Ayca and Lynett (2016) studied the effects of tsunami-induced currents to assess the hazard in California's ports and harbors.

For earthquake-generated tsunamis, THA studies typically break down the earthquake sources into near field and far field (e.g., Gonzalez et al. 2009). For the near-field sources, for which the details of the rupture process affect the run-up distribution, a wide range of source mechanisms and slip distributions is considered to capture the uncertainty of the source characterization for a given earthquake magnitude. For the far-field sources, the details of the rupture process have less of an effect on run-up distribution, and the major factors become the earthquake magnitude and source location. The choice of earthquake scenarios with a wide range of magnitudes is used to infer the tsunami hazard across the return periods considered.

In the particular case of characterizing the hazard for sensitive infrastructure, the tail of the hazard curve that corresponds to long return period events becomes crucial. Consequently, there is an inevitable need to define extreme-but-probable events that adhere to the current understanding of seismicity and tectonics. This is a sensitive subject that eventually leads to the question of "what is the worst probable scenario?" In answering this question, the seismo-tsunami community has been very cautious in designing unsubstantiated extreme earthquake scenarios for subduction zones for which the historical record is short and for which there is lack of concrete evidence of past mega-earthquake events. Some of the subduction zones thought to be incapable of producing mega events have eventually presented evidence of the opposite, in some occasions through the discovery of field evidence (e.g., the Cascadia SZ) and in other occasions through the manifestation of unexpected modern-day catastrophes. The 2004 and 2011 events highlighted the danger of

discarding the probability of mega-earthquake events occurring in other "dormant" subduction zones, which bear the capacity to produce such events. This notion led to the studies of McCaffrey (2008) (MC08), Berryman et al. (2015) (GEM15) and Rong et al. (2014) (RO14), which assign maximum and probable maximum earthquakes to all major subduction zones. Rong et al. (2014) demonstrated that M9 earthquakes could occur on any circum-Pacific subduction zone within a very long time frame (in the order of ~10,000 years).

This study uses the worst-case scenario approach, utilizing the proposed maximum magnitude earthquake scenarios along the Pacific subduction zones, taking it one step further to determine the Probable Maximum Tsunami (PMT) in Central California. The western USA, bordered by the Alaska–Aleutian and Cascadia subduction, is very susceptible to catastrophic events similar to these of 2004 and 2011. A sensitivity analysis is performed to determine which subduction zone generates the largest wave amplitude offshore of Pismo Beach, which can be applied for any other coastal site along the Pacific. This study region is chosen because it is representative of the central Californian terrain and is away from major subduction zones. The case study results and the simplifications involved in the methodology are discussed.

2 Methods

This section will succinctly provide information about the proposed methodology to determine the worst-case scenario for any particular subduction zone. Section 2.1 describes the unit sources database used in the analysis. Section 2.2 describes two approaches to assign maximum probable magnitude earthquakes to each subduction zone and infer appropriate rupture areas/slip magnitudes based on three relevant publications: MC08, GEM15 and RO14. Sections 2.3 and 2.4 describe the numerical model and grids used. Finally, Sect. 3 presents a case study for Central California where the tsunami hazard of the maximum magnitude earthquake sources is assessed and the two worst-case scenarios are discussed.

2.1 NOAA tsunami unit source database

The Pacific Marine Environmental Laboratory (PMEL) of the National Oceanic and Atmospheric Administration (NOAA), as part of their real-time tsunami forecasting system, has discretized the circum-Pacific subduction zones into sub-faults of size 100×50 km (along-strike length $\times$ along-dip width). The sub-faults are prescribed a strike angle that more-or-less follows the inter-plate boundary (Bird 2003). The dip angle and the down-dip extend of the unit sources are based on the best knowledge of local fault geometry (e.g. Kirby et al. 2005). Figure 1 shows the sub-faults and the NOAA labeling for the Japan subduction zone. The numbers represent the source column numeral which runs along the subduction zone and the letters in front of the numbers represent the source row name in the down-dip direction. The rows go from shallowest to deepest in the following order: B, A, Z, Y, X, W, V, whereas rows C and D represent normal faulting unit sources. Finally, the sources are assigned a four-lettered code, depending on which subduction zone they are part of (see Table 1). For more details about the source location and parameters, see Gica et al. (2008) and Tang et al. (2010).

Fig. 1 NOAA's unit sources and labeling along the Japan subduction zone (KISZ)

Table 1 Subduction zone four-letter labeling used for the NOAA tsunami unit sources (Tang et al. 2010)	Subduction zone	NOAA 4-letter code
	Alaska–Aleutians–Cascadia	ACSZ
	Central and South America	CSSZ
	Eastern Philippines	EPSZ
	Kamchatka-Kuril-Japan-Izu-Mariana-Yap	KISZ
	Manus-Oceanic Convergent Boundary	MOSZ
	New Guinea	NGSZ
	New Zealand–Kermadec–Tonga	NTSZ
	New Britain–Solomons–Vanuatu	NVSZ
	Ryukyu–Kyushu–Nankai	RNSZ

For the purpose of tsunami modeling, rake angle is fixed at 90°, thus representing pure thrust rupture, which is a conservative assumption and assumes full strain partitioning at oblique subduction zones (McCaffrey 1992). The surface deformation from the rupture of each sub-fault has been computed using Okada's (1985) analytical formulas for 1 m slip magnitude, thus calling them *unit sources*. The tsunami amplitudes and velocities across the Pacific basin were computed using the *MOST* hydrodynamic model (see Sect. 2.3) on a 4 arc-min grid and have been stored in an on-line database at 16 arc-min resolution. Since surface deformation and deep-water propagation are a linear function of slip magnitude, the tsunami amplitudes across the Pacific Ocean can be readily obtained for any

combination of unit sources and slip magnitudes. Therefore, the variation of slip magnitude during seismic rupture can be accounted for by creating more complex faulting scenarios (Titov et al. 1999). This linear property of deep-water tsunami propagation is the basis of NOAA's tsunami source inversion procedure during real-time tsunami forecasts (Percival et al. 2009).

2.2 Far-field source specification

Since the study area described in Sect. 3 is located in Central California, it is immediately evident that only sources around the Pacific Ocean are considered in the analysis. The maximum energy from the Cascadia subduction zone (CSZ) beams away from the coast of California. Therefore, California only gets the edge waves that are propagating orthogonal to the main propagation axis. For this reason, the sources from the CSZ will be considered as far field in the analysis of the present study.

The size of any earthquake event is quantified from the seismic moment, defined as

$$M_0 = \mu L_R W_R u_{av}, \tag{1}$$

where μ is the earth's rigidity (typical values range between 30 and 45 GPa at depths 20–45 km along the subduction zone interface, Bilek and Lay 1999), L_R and W_R are the fault rupture length and width, and u_{av} is the average slip magnitude. Moment magnitude M_w can be computed from the seismic moment M_0 (defined in units of N m) as (Hanks and Kanamori 1979)

$$M_w = \frac{2}{3}\log(M_0) - 6.07. \tag{2}$$

To obtain the maximum probable earthquake magnitude for each subduction zone, we refer to the following three publications previously mentioned: MC08, GEM15, and RO14. In the first two publications (MC08, GEM15), the subduction zones are divided in discrete sections and for each section a maximum possible magnitude (m_x) is assigned based on the length of the segment L and the seismogenic layer thickness considered. MC08 assigned a fixed fault depth of $d = 40$ km, whereas GEM15 assign fault segment-specific seismogenic layer depth d (vertical distance from down-dip extent to up-dip edge). The subduction zone width W is then calculated from $W = d/\sin(\delta)$, using a subduction zone/fault segment-specific dip angle δ. The along-strike segment boundaries are defined based on plate kinematic information and/or from the presence of geological barriers, which are open to interpretation. Features previously thought to be barriers during earthquake rupture have been crossed, such as the Australian-Woodlark-Pacific triple plate junction, which was crossed during the 2007 $M_w8.8$ Solomon Island earthquake (Taylor et al. 2008). To calculate the slip magnitude, MC08 and GEM15 employed the formula (Liu-Zeng et al. 2005)

$$u_{av} = 2.5 \pm 1.0 \times 10^{-5} \text{ L} \approx 2.5 \times 10^{-5} \text{ L}, \tag{3}$$

which is based on the extrapolation of the Wells and Coppersmith (1994) scaling relations. The earth's rigidity was set in both studies equal to $\mu = 30$ GPa for all subduction zones.

In the case of implementing a frequency-magnitude relation, such as the Tapered Gutemberg–Richter (*TGR*) relation that RO14 used, maximum magnitude is defined relative to a time frame. This allows a more realistic definition for m_x, the *maximum probable magnitude* m_p (*T*). Even though the *TGR* distribution is truncated at the tail of the

Gutemberg-Richter (G-R) distribution and is constrained by the moment rate conservation principle, it is greatly affected by statistical errors generated from the limited sample at higher earthquake magnitudes (Geist and Parsons 2014; Kagan 2002). For the Cascadia subduction zone, RO14 utilized the 10,000-year turbidity record of Goldfinger et al. (2012), which is complete for magnitudes above 8–8.5, so as to extend the seismic catalog beyond the instrumental period. However, for other subduction zones, very little paleo-seismic information exists to constraint the tail of the *TGR* distribution. In addition, there is a debate of whether the *β* (index parameter of the distribution) parameter should be global, i.e., using global earthquakes from the seismic catalog, or zone specific (RO14 and references therein). In the case of zone-specific, it can be argued that the distribution is more fitting to a particular faulting regime and tectonic setting, but at the same time the earthquake event sample is significantly reduced (Bird and Kagan 2004).

The segment ruptures of MC08 and GEM15 can be assigned a return period using $T = \frac{u_{av}}{f \times v}$, where u_{av} is the average slip magnitude, v is the plate convergence rate, f is the fraction of the total seismic moment in M9 earthquakes, and χ is the fraction of slip on the boundary that occurs seismically (also called the *seismic coupling coefficient*). The recurrence times estimated by MC08 for the maximum magnitude events range between hundreds to thousands of years. On the other hand, RO14's maximum probable earthquake is readily expressed in terms of a return period.

The maximum earthquake magnitude for each Flinn–Engdahl (F–E) zone is sought by taking the maximum between $m_p(10,000)$ from RO14, $m_x - max$ from the GEM15 report and the maximum magnitudes reported by MC08. GEM15 provide alternative definitions of maximum magnitude for each subduction zone (*minimum*, *maximum*, and *preferred*, the last being the average between *minimum* and *maximum*), and $m_x - max$ corresponds to the maximum. In the GEM15 report, irrespective of the size of identified continuous fault segments, $m_x - max$ was universally limited at 9.6, to what the authors define as the "generally accepted maximum magnitude," and $m_x - max$ for Cascadia was limited to 9.2 to be consistent with the findings of Frankel and Petersen (2008). Figure 2 shows a
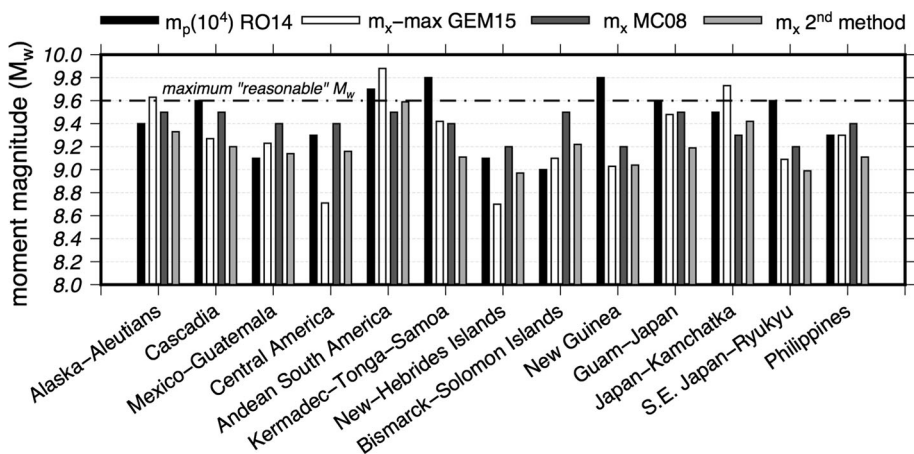

Fig. 2 Comparison of maximum seismic magnitudes for all circum-Pacific F-E zones. Adapted from figure 9 of Rong et al. (2014), with the difference that the $m_p(10,000)$ is the highest between zone-specific and generic *β* values, and we've added the maximum magnitudes from the second methodology of this study (m_x *2nd method*)

comparison between the maximum earthquake magnitudes (without curtailment) found in the reference studies. The GEM15 $m_x - max$ is relatively low for Central America and New-Hebrides-Samoa subduction zones, whereas $m_p(10,000)$ is relatively large for the New Guinea and Kermadec–Tonga–Samoa subduction zones (9.8 M). Moment magnitudes for the rest of the subduction zones compare well.

In the absence of a definite argument on which maximum expected/probable magnitude to assign to each subduction zone, it is conservative to select the maximum reported for each F-E zone. However, the authors recognize that the maximum magnitude curtailment to a "generally accepted maximum magnitude" remains open for interpretation and needs to be addressed here. Moreover, there are several scaling relations available in the literature to compute slip magnitude. As opposed to Eq. 3, which is based on magnitude-limited ($\sim M8$) crustal earthquake events, the more recent scaling relations of Strasser et al. (2010), Blaser et al. (2010) and Murotani et al. (2013) have been developed specifically for subduction zone earthquakes. Using the scaling relations for subduction zone earthquakes has a direct effect on the maximum magnitudes assigned to each F-E zone.

Considering the above, we propose two alternative methodologies to design maximum magnitude earthquake scenarios: i) a methodology that assigns earthquake scenarios found in the literature that maximize the source's tsunami generation potential, and ii) a methodology that assigns maximum magnitudes based on the scaling relations for subduction zone earthquakes. We outline the two methodologies in the following sections. Due to the fact that tsunami generation is directly linked to the co-seismic vertical surface deformation, the slip magnitude controls, in a large extent, the tsunami generation. In the near field, slip magnitude and distribution control the tsunami run-up (Okal and Synolakis 2004). However, for far-field sources, the details of slip distribution are less important (Okal and Synolakis 2008), and it becomes reasonable to assume a uniform slip model in both methodologies.

2.2.1 Methodology for "maximum tsunami generation"

In this methodology, we identified earthquake scenarios reported in the literature that maximize the tsunami generation potential. We selected the maximum earthquake magnitude reported by MC08, RO14 and GEM15 for each F-E zone, with no moment magnitude limit applied. We employed Eq. 3 for the calculation of slip magnitude using the upper limit, i.e. $u_{av} = 3.5 \times 10^{-5}$ L. The earth's rigidity was taken as a constant and equal to the conservative value of $\mu = 30$ GPa. Both assumptions were made to maximize the tsunami amplitude given an earthquake magnitude. We used the maximum rupture areas (length and width) provided in MC08 and GEM15 as a guide to assign the fault rupture source parameters (Table 2). In some cases, the length and width of the subduction zone were limited (e.g. NGSZ) therefore a larger slip magnitude ($u_{av} > 3.5 \times 10^{-5}$ L) was used to match the maximum magnitude assigned.

2.2.2 Methodology to assign "reasonable" maximum magnitudes and average slip

In this methodology, we utilized scaling relations for subduction zone earthquakes to obtain maximum earthquake magnitudes using the maximum fault rupture areas reported in MC08 and GEM15 for each F-E zone. It can be argued that Eq. 3 is not an appropriate scaling relation for slip magnitude, since it is based on a sample of magnitude-limited crustal earthquake events of strike-slip nature (Liu-Zeng et al. 2005). Slip magnitude has a

Table 2 Maximum seismic magnitudes, length, and width for selected subduction zones

Subduction zone code	Location	GEM15	Length (km)	Width (km)	MC08	Length (km)	Width (km)	RO14 m_p (10,000)
AASZ	Alaska	9.6 (**9.63**)	1963	123	9.5	1489	129	9.4
AASZ	Cascadia	9.2 (9.27)	1415	68	9.5	1048	256	**9.6**
CSSZ	Mexico	9.23	1710	40	**9.4**	1378	112	9.1
CSSZ	C. America	8.71	533	68	**9.4**	1506	107	9.3
CSSZ	S. America	9.6 (**9.88**)	2502	178	9.5	1304	178	9.7
NTSZ	Kermadec	9.42	1627	87	9.4	1450	98	**9.8**
NGSZ	N. Guinea	9.03	764	100	9.2	1030	117	**9.8**
KISZ	Guam-Japan	9.48	1822	85	9.5	1812	95	**9.6**
KISZ	Kamchatka-Japan	9.6 (**9.73**)	2223	134	9.3	1242	91	9.5
RNSZ	Rykukyu	9.09	1440	35	9.2	1131	95	**9.6**

Numbers in parentheses indicate maximum magnitudes before curtailment. The maximum magnitude of the three studies for each subduction zone is shown in boldface

direct effect on the estimated maximum magnitudes reported in MC08 and GEM15. Here, we re-calculated the maximum magnitudes using the scaling relations of Strasser et al. (2010) and Blaser et al. (2010) and Murotani et al. (2013) and assigned the maximum magnitude resulting from the application of the scaling relations to each F-E zone. In all F-E zones, the Blaser et al. (2010) scaling relations generated the highest magnitude. For Cascadia, the moment magnitude was curtailed at 9.2, as in GEM15. The suggested fault rupture areas were fit to the unit source database, and the slip magnitude was computed from Eq. 1, using the conservative earth's rigidity value of $\mu = 30$ GPa. It should be noted that rupture lengths above 1400 km considered here fall outside the range of validity of the scaling relations and therefore the corresponding results should be used with caution.

2.2.3 Source specification and scaling

The magnitude, rupture area and slip magnitude of the far-field sources considered in this report using the two aforementioned methodologies are given in Tables 3 and 4. It is notable that slip resulting from the application of scaling relations for subduction zone earthquakes is significantly lower compared to the slip assigned using Eq. 3 and consequently maximum earthquake magnitudes following the second methodology are significantly lower (Fig. 2).

The unit sources corresponding to each source are also provided using NOAA/PMEL's labels (fault specification column in Tables 3, 4). Since the unit source size is pre-defined, the dimensions of the fault rupture area for each earthquake scenario are multiples of 100 km along-strike, times multiples of 50 km along-dip. The rupture width was either kept constant (scaled either upward or downward from the suggested width to the closest multiple of 50 km) or varying across the rupture length (with the suggested width approximately matched by the mean). In the first methodology, rupture length and slip magnitude were coupled through Eq. 3, and were selected so as to produce the desired maximum moment magnitude. In the second methodology, the rupture length resulted

Table 3 Source Specification for Earthquake scenarios modeled in this study using the methodology for "maximum tsunami generation"

Source	Subduction zone	Location	M_w	Length (km)	Width (km)	Slip (m)	Fault model specification*
AA-1	ACSZ	Alaska	9.6	1500	150	52.5	a22-a36, b22-b36, z22-z36
AA-2	ACSZ	Alaska	9.6	1700	100	59.5	a20-a36, b20-b36
CAS-1	ACSZ	Cascadia	9.6	1500	Varies	52.5	a51-a65, b51-b65, z55-z62
CAS-2	ACSZ	Cascadia	9.6	1700	100	59.5	a49-a65, b49-b65
CAS-3	ACSZ	Cascadia	9.6	1400	Varies	Varies	50 m*(a52-a56, b52-b56) + 60 m*(a57-a60, b57-b60, z57-z60) + 70 m* (a61-a63, b61-b63, z61-z62) + 80 m*(a64-a65, b64-b65)
ME-1	CSSZ	Mexico	9.4	1100	100	38.5	a1-a11, b1-b11
CA-1	CSSZ	C. America	9.4	1100	100	38.5	a15-a25, b15-b25
SA-1	CSSZ	Peru	9.9	2500	Varies	87.5	a49-a73, b49-b73, z49, z53-63, z67-73
SA-2	CSSZ	C. Chile	9.9	2500	Varies	87.5	a72-a96, b72-b96, z72-73, z88-z96
SA-3	CSSZ	S. Chile	9.9	2500	Varies	87.5	a83-a107, b83-b107, z88-z107
KT-1	NTSZ	Kerdmadec	9.8	2500	100	87.5	a12-a36, b12-b36
NG-1	NGSZ	N. Guinea	9.8	1500	100	120	a1-a15, b1-b15
NG-2	NGSZ	N. Guinea	9.8	1200	100	150	a1-a12, b1-b12
GJ-1	KISZ	Marianas	9.6	1800	100	63	a44-a61, b44-b61
GJ-2	KISZ	Marianas	9.6	1800	100	63	a34-a51, b34-b51
JK-1	KISZ	Kurils	9.7	2200	100	77	a1-a22, b1-b22
JK-2	KISZ	Kurils	9.7	1700	150	59.5	a2-a18, b2-b18, z2-z18
RN-1	RNSZ	Ryukyu	9.6	1800	100	63	a4-a21, b4-b21

from complying with the recommended rupture areas (to the closest multiple of 100 km). Sources AA-5 and AA-6 were assigned a smaller rupture area than the recommended maximum, allowing for an increase in slip given the same moment magnitude; for this case area-slip scaling relations are relaxed to maximize tsunami generation while maintaining the target moment magnitude. For Cascadia, which is the closest subduction zone to the study area, we included two sources that were assigned variable slip magnitude along-strike, with the maximum slip assigned to the southern-most unit sources that beam the most energy to the site.

The segmentation of the subduction zones in MC08 and GEM15 is based on changes in the direction, rate of plate convergence, and/or natural geologic breaks. For some of the subduction zones considered, the maximum length segments were re-positioned in places where more tsunami energy beams toward the site. This decision is based on the argument that such boundaries have been crossed in the past. The following section presents an implementation of the methodologies presented so far.

Table 4 Source Specification for Earthquake scenarios modeled in this study using the methodology assigning "reasonable maximum magnitudes"

Source	Subduction zone	Location	M_w	Length (km)	Width (km)	Slip (m)	Fault model specification*
AA-3	ACSZ	Alaska	9.3	1600	150	17.7	a23-a38, b23-b38, z23-z38
AA-4	ACSZ	Alaska	9.3	1900	Varies	17.7	a20-a38, b20-b38, z29-z38
AA-5	ACSZ	Alaska	9.3	1400	100	30.0	a24-a37, b24-b37
AA-6	ACSZ	Alaska	9.3	900	150	31.0	a29-a37, b29-b37, z29-z37
CAS-4	ACSZ	Cascadia	9.2	1400	100	19.2	a52-a65, b52-b65
CAS-5	ACSZ	Cascadia	9.2	800	150	22.4	a55-a62, b55-b62
CAS-6	ACSZ	Cascadia	9.2	1400	100	Varies	10 m*(a52-a54, b52-b54) + 15 m*(a55-a57, b55-b57) + 20 m* (a58-a61, b58-b61) + 29 m*(a62-a65, b62-b65)
ME-2	CSSZ	Mexico	9.1	1500	100	14.7	a1-a15, b1-b15
CA-2	CSSZ	C. America	9.2	1600	100	14.6	a15-a30, b15-b30
SA-4	CSSZ	Peru	9.6	2600	Varies	23.2	a48-a73, b48-b73, z48-z49, z53-z63, z67-73, y48-49, y53-y62, y69-y71, x56-x57
SA-5	CSSZ	S. Chile	9.6	2500	Varies	23.2	a87-a111, b87-b111, z88-z111, y96-110
KT-2	NTSZ	Kerdmadec	9.1	1500	100	13.0	a22-a36, b22-b36
NG-3	NGSZ	N. Guinea	9.0	1200	100	12.8	a1-a12, b1-b12
GJ-3	KISZ	Marianas	9.2	1700	100	15.2	a32-a48, b32-b48
JK-3	KISZ	Kurils	9.4	2000	150	19.2	a1-a20, b1-b20, z1-20
RN-2	RNSZ	Ryukyu	9.0	1100	100	11.9	a11-a21, b11-b21

2.3 Tsunami modeling

In this work, the *Method Of Splitting Tsunami* (MOST) hydrodynamic model is implemented through the ComMIT interface. *MOST* was introduced by Titov and Synolakis (1995, 1998), has been extensively validated and used for tsunami hazard assessments in the USA (Wei et al. 2012, Synolakis et al. 2008; Titov and González 1997) and is currently maintained and in operational use at NOAA/PMEL for propagation and inundation forecasting (Titov 2009). ComMIT (Community Modeling Interface for Tsunamis) is a Web-enabled interface (Titov et al. 2011) that uses MOST for the hydrodynamic computations and allows the user to utilize the unit sources database. Variants of the *MOST* model have been in constant use for tsunami hazard assessments in California since the mid-1990s.

MOST solves the 2 + 1 Nonlinear Shallow Water equations (NSWE):

$$h_t + (uh)_x + (vh)_y = 0, \tag{4}$$

$$u_t + uu_x + vu_y = g\eta_x - Du, \tag{5}$$

$$v_t + uv_x + vv_y = g\eta_y - Dv, \tag{6}$$

where $\eta(x, y, t)$ is the wave amplitude, d is the water depth, $h(x, y, t) = \eta(x, y, t) + d(x, y, t)$, $u(x, y, t)$ and $v(x, y, t)$ are the depth-averaged velocities, and $D(h, u, v)$ is the drag coefficient computed by:

$$D(h, u, v) = n^2 g h^{-4/3} \sqrt{u^2 + v^2}, \tag{7}$$

where n is the Manning's friction coefficient.

MOST solves the NSWE and so is intrinsically non-dispersive, although for certain grid configurations the numerical dispersion of the MOST solution scheme can approximately match physical dispersion (Burwell et al. 2007). Nevertheless, the SW approximation is valid for earthquake-generated tsunamis for which the wavelengths are at least 20 times greater than the oceanic water depth. Wave breaking is not physically modeled in MOST, but the inherent numerical dissipation at the breaking point reflects the wave breaking evolution adequately (Titov and Synolakis 1998).

Run-up and inundation are only predicted in the higher resolution grid (1/3 arc-sec or approximately 10 m). A Manning's coefficient of $n = 0.03$ s/m$^{1/3}$ (corresponding to a "weedy earth channel" surface) is used, constant throughout the grid. The choice of friction coefficient should ideally be validated using field data from past events when available for a study area. In this case, in the absence of such data, the authors used their best judgment to select an appropriate friction coefficient. The run-up values for steep topographies, such as in the area of this study, are not expected to be significantly affected by the choice of friction coefficient (Tang et al. 2009).

2.4 Numerical grids

The shoaling effects of wave evolution over the continental shelf and slope require the decrease in the spatial size of the numerical grid to accurately resolve the steepening wave profiles (nonlinearity). In the finite-difference scheme employed by *ComMIT*, the shoaling effect is accounted for by using three nested grids of increasing spatial resolution. The coarsest grid (grid A) which covers the largest area has a resolution of 12 arc-sec, whereas the intermediate (grid B) and finest grid (grid C) have a spatial resolution of 3 arc-sec and 1/3 arc-sec (≈ 10 m), respectively, (see Table 5). Grid C was obtained from the freely available database of the National Centers for Environmental Research's (NCEI) Tsunami Inundation Digital Elevation Models (DEM's) (Friday et al. 2011). Grid B was acquired from the Coastal Relief Model (CRM), available in the NCEI database. The coarsest grid, grid A, was obtained from the *FACTS* (Facility for the Analysis and Comparison of Tsunami Simulations) database. This grid was used by Barberopoulou et al. (2009) to

Table 5 Nested grids of increasing resolution (grid A: 12 arc-sec; grid B: 3 arc-sec; grid C: 1/3 arc-sec) used for the numerical computations

	Lon. Range (°E)	Lat. Range (°N)	Nx	Ny	$\Delta x/\Delta y$	Δt (sec)
Grid A	238.7700–239.5600	34.7075–35.5375	238	250	12″	3
Grid B	239.0000–239.3000	35.0000–35.3108	361	374	3″	0.75
Grid C	239.1203–239.1666	35.1814–35.2277	501	501	1/3″	0.25

produce the tsunami inundation maps of the State of California. All the grids are referenced to the Mean High Water (MHW) vertical tidal datum and to the World Geodetic System of 1984 (WGS 84) horizontal datum, in spherical coordinates. The time step for each grid satisfies the Courant–Friedrichs–Lewy (CFL) condition, which necessitates that information travels faster than the wave propagation speed in the domain: $\Delta t \leq \Delta x / C_{\max}$, where Δt is the time step, Δx is the grid spacing and $C_{\max}$ is the maximum water speed in the domain (i.e. $C_{max} = \sqrt{gh_{\max}}$, following the notation used in Eqs. 4–7).

3 Case study

3.1 Far-field sources

As it was previously mentioned, only sources around the Pacific Rim are considered since Central California's coast faces the Pacific Ocean. For different areas of interest, other sources may apply. The subduction zones considered in the analysis are shown in Fig. 3. To identify which subduction zones direct more energy toward Central California, a sensitivity analysis was done utilizing the NOAA/PMEL unit sources database. Tsunami
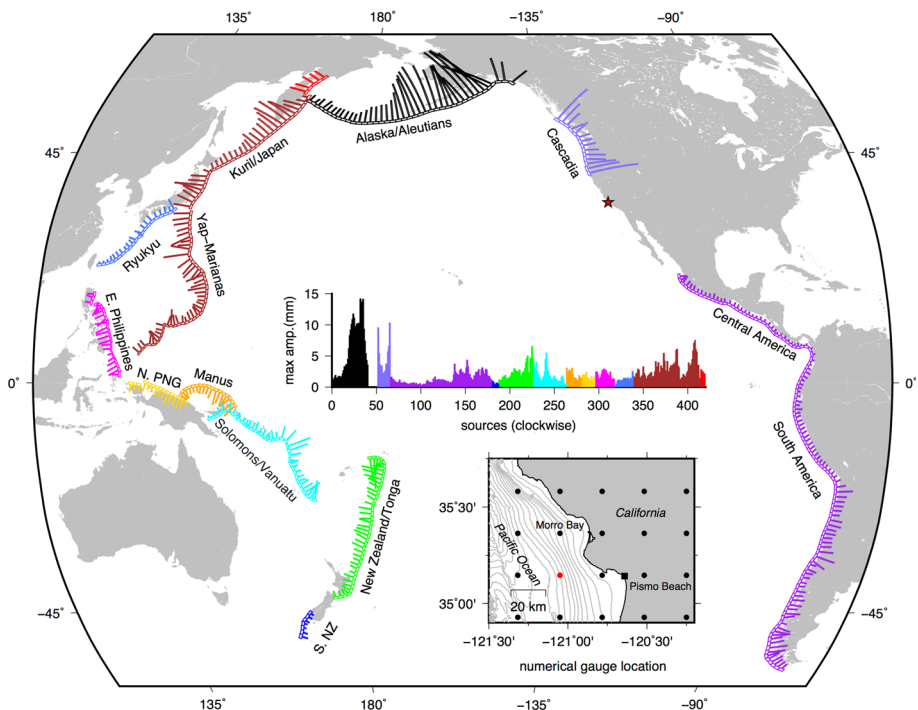
Fig. 3 Tsunami hazard sensitivity for Central California to the location of the unit sources (only shallowest thrust unit sources shown here). The lengths of the bars show the relative maximum amplitude offshore of Pismo Beach/southwest of Morro Bay from each unit source. The numerical gauge location inset figure shows the propagation database grid points near the site with 16 arc-min spacing (*black circles*) and the location of the chosen numerical gauge for the sensitivity analysis (*red circle*). The other inset figure shows the maximum amplitude values, moving clockwise around the Pacific Ocean, starting from W. Aleutians and ending at N. Kamchatka

amplitude time series for all the unit sources are available at discrete nodes with 16 arc-min spacing. Figure 3 was developed by selecting an offshore node off Pismo Beach (shown in inset of Fig. 3) and saving the maximum (positive) amplitude produced from each unit source. The maximum positive amplitudes are plotted for all the row B (shallowest) unit sources. This analysis readily illustrates that the unit sources from the Alaska–Aleutian and Cascadia subduction zones produce the largest amplitudes offshore, with Alaska–Aleutians subduction zone producing the highest. These results confirm the findings of Uslu (2008), that Northern and Central California are more susceptible to tsunami from these two subduction zones.

All unit sources have the same dimensions, the same slip magnitude, and consequently the same moment magnitude (assuming earth's rigidity μ is constant everywhere). Therefore, it is important to stress that the sensitivity analysis performed does not take into account the largest possible magnitude earthquake for each subduction zone. Also, the unit sources have been assigned a pure thrust mechanism that does not necessarily reflect the nature of all subduction zones considered here. Figure 3 only identifies the variability of maximum amplitude between sources due to differences in the fault geometry (dip angle), the distance from source to site, and the oceanic bathymetry/topography that refracts/reflects the waves and dictates where the tsunami energy is beamed (directivity). Consequently, it cannot be immediately determined, without taking maximum possible earthquake magnitudes and more appropriate mechanisms (for certain subduction zones of oblique nature) into consideration, where the worst-case tsunami source for Central California is. Nevertheless, it provides a strong indication that the Alaska–Aleutian subduction zone presents the highest risk to the study area. A detailed description of this subduction zone is provided in the following section.

3.1.1 Alaska–Aleutians subduction zone (AASZ)

The Alaska–Aleutian subduction zone (AASZ) is one of the two major tsunamigenic zones in the continental US, along with Cascadia. It has produced major earthquakes in the past that resulted in trans-oceanic tsunamis. The three most notable earthquakes in the region, during the instrumental period, are the 8.2 M_w 1946 Aleutian Islands (Johnson and Satake 1997), 8.6 M_w 1957 Andreanof Islands (Johnson et al. 1994) and 9.2 M_w 1964 Prince William Sound (Plafker 1969; Kanamori 1970) earthquakes.

The 8.2 M_w 1946 earthquake is well known for the disproportionate—to the size of the earthquake-generated tsunami. The tsunami was catastrophic both in the near field and far field. In the near field, it destroyed in the Scotch Cap lighthouse in Unimak Island, where run-up reached 42 m (Okal et al. 2003). The enhanced near-field run-up of this particularly tsunamigenic earthquake with the typical characteristics of *tsunami earthquakes* (Kanamori 1972), has been attributed to the triggering of a local landslide (Okal et al. 2003; López and Okal 2006; Okal and Hébert 2007). In the far field, the generated tsunami impacted coastal areas as far as Marquesas Islands of French Polynesia and caused 159 casualties in Hilo, Hawaii (Fuchs 1982). In Hawaii Islands, waves reached 11.3 m in Oahu and 16.8 m in Hilo (Loomis 1976), resulting in 159 casualties in Hawaii (USC website). In California, a 0.9-m amplitude wave was reported in Crescent City, whereas the most damaging effects were noted in Half Moon Bay, where the waves *shoved boats nearly 304.8 m inland* as the water level rose 3 m above the original level (Lander et al. 1993).

The 8.6 M_w Great Aleutian Island earthquake occurred in March 9, 1957, in the Aleutian Island arc (Wesson et al. 2007). The earthquake ruptured 1200 km along the Aleutian Trench, and is one of the longest ruptures ever recorded from aftershocks

(Johnson et al. 1994). In near field, there was no damage reported, as most of the Aleutian Islands are uninhabited (USC website). In the far field, the generated tsunami reached 16.1 m in Kauai, 6.7 m in Oahu and 9.8 m in Hawaii Isl. (Loomis 1976), without causing any casualties. In California, damage estimated at $5000 was reported in San Diego, as the waves arrived in the form of a late surge with currents reaching 48.3 km/h (Lander et al. 1993).

The Good Friday 1964 earthquake, by the shear size of the energy released, caused widespread destruction in the near field and generated a trans-Pacific tsunami. The magnitude of the earthquake that left 114 death or missing (Grantz et al. 1964) was evaluated at 9.2 M_w (7.5×10^{29} dyne-cm) by Kanamori (1970) using long-period surface waves, rendering it to be one of the three largest earthquakes recorded after the 9.6 M_w 1960 Chilean and 9.3 M_w 2004 Sumatran earthquakes (Chlieh et al. 2007). Plafker (1969, 1972) measured surface deformation in the near field to propose a fault rupture of 800 km long, 175–290 km wide, dipping at 9° and with 20 + m of slip in the eastern part of the Alaskan subduction zone. The generated tsunami waves were particularly destructive in Kenai Peninsula and the Kodiac Islands group where an initial sea withdrawal was reported and peak crest elevation reached 9.1 m (Grantz et al. 1964). Run-up in the Gulf of Alaska reached 18–30 m, with the maximum of 27–30 m above mean lower low tide were reached near the head of Aialik Bay (Wilson and Torum 1968). In Hawaii, waves generally reached around 2 m with a maximum of 4.6 m in Oahu Isl. (Loomis 1976). In California run-up was pronounced in the northern part, reaching 6.1 m in Crescent City, and decreased moving south to 3 m in San Francisco Bay and 3.8 m in Santa Cruz (Wilson and Torum 1968). The decay of the tsunami wave height (north to south) along the Californian coast is also evident in the tide gauge records shown in Table 6. Furthermore, the earthquake triggered around 20 local submarine and subaerial landslide tsunamis in Alaska, which led to the majority of the tsunami fatalities (Lander 1996). At the town of Seward, the highest locally wave height was 6–8 m and hit the waterfront about 1.5–2.0 min after the shaking began (Suleimani et al. 2011).

3.1.2 Zonation

The biggest part of the Alaska–Aleutians Arc has ruptured in the past century (Wesson et al. 2007). The two exceptions are the west part of the Aleutian Trench near the Komandorksi Islands (west of the 1965 rupture area), and near the Shumagin Islands (between the 1938 and 1957 rupture areas). Near Komandorksi Islands, subduction is taking place at an oblique angle and it is not clear if it is capable of producing large earthquakes (Wesson et al. 2007 and references therein). That section of the Arc does not pose a big threat to the Central California due to directivity of tsunami propagation across

Table 6 Maximum rise or fall (in meters) at the tide stations in California for tsunami events between 1946 and 1964. *Source* Spaeth and Berkman (1965)	Station	1946	1952	1957	1960	1964
	Crescent City	1.8	2.1	1.3	3.3	4.0+
	San Francisco	0.5	1.1	0.5	0.9	2.3
	Santa Monica		1.1	0.9	2.8+	2.0
	Los Angeles	0.8	0.6	0.6	1.5	1.0
	La Jolla	0.4	0.2	0.6	1.0	0.7
	San Diego	0.4	0.7	0.5	1.4	1.1

the ocean. For the Shumagin Islands *seismic gap*, on the other hand, it has been found that the seismic coupling is very low and most of the slip is aseismic (Freymueller and Beavan 1999, 2007). In the zonation of MC08, the Alaska–Aleutians Arc is divided in three segments: W. Aleutians, with $L = 1244$ km; E. Aleutians, with $L = 1092$ km; and Alaska, with $L = 1489$ km (see Fig. 4). Since MC08 does not provide more detailed information where the segments start and finish, the three segments are distributed along the arc. The Alaskan segment is interpreted by the authors as overlapping the Shumagin seismic gap. The GEM15 zonation, which follows that of Wesson et al. (2007), has the Shumagin gap as a separate segment, and the Arc east of Shumagin is divided into three more segments. This zonation was done based on kinematic data and for the purpose of accommodating smaller magnitude ($\approx M8$) events for the seismic hazard assessment study of Wesson et al. (2007). However, Wesson et al. (1999, 2007) assumed in their analysis that no large earthquake will rupture through the Shumagin segment (using the term *extremely unlikely*).

3.1.3 Selected maximum magnitude sources

From Fig. 2 and Table 2 the maximum magnitude for the AASZ is 9.63 M_{w}, found in GEM15. Based on this magnitude, two sources are proposed of length $L = 1500$ km and $L = 1700$ km and width $W = 150$ km and $W = 100$ km, respectively, (sources AA-1 and AA-2 in Table 3). The width of the sources is above and below the preferred width $W = 123$ km of GEM15 (Table 2). The moment magnitude of source AA-1 matches the 9.63M_{w} in GEM15, whereas source AA-2 is assigned a smaller moment magnitude (9.59M_{w}), albeit with higher slip magnitude. The high slip of $u_{\mathrm{av}} \sim 60$ m for source AA-2 has been suggested to have occurred during the slip history of the 2011 Tohoku earthquake (Shao et al. 2011).

Following the second methodology of assigning maximum earthquakes magnitudes to SZs (Table 4), the maximum magnitude for the AASZ is 9.33 M_{w}, using the maximum fault rupture area proposed in GEM15 and the scaling relations of Blaser et al. (2010). Based on this magnitude we propose four sources AA-3, AA-4, AA-5, and AA-6. Sources AA-3 and AA-4 are assigned the maximum fault rupture area found in GEM15, and the slip magnitude resulting from the application of the Blaser et al. (2010) scaling relation. Sources AA-5 and AA-6 are assigned smaller rupture areas and higher slip magnitudes to maximize tsunami generation, keeping moment magnitude constant.

Along dip, all sources are positioned in the shallowest part of the trench to maximize the vertical surface deformation, and consequently the tsunami generation efficiency. In the along-strike direction, all AA sources are placed in the part of the AASZ that beams the
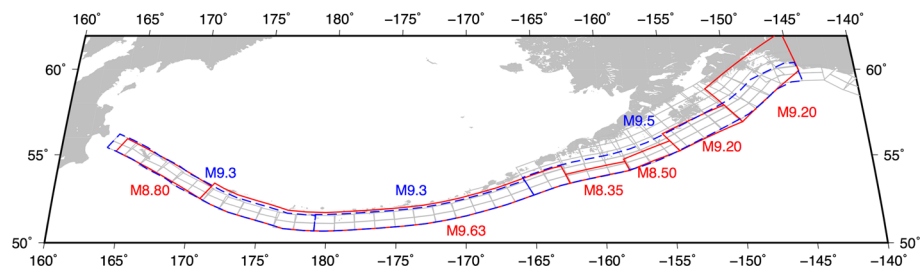

Fig. 4 Alaska–Aleutian subduction zone segments as defined by MC08 (*blue dashed lines* and *blue font*) and GEM15 (*red solid lines* and *red font*). NOAA's unit sources are shown with the *gray rectangles*

most tsunami energy toward Pismo Beach/southwest of Morro Bay (Fig. 5). Note that small variations in the location of the source may lead to differences in the resulting run-up distribution in the study area. With the exception of source AA-6, all other AASZ sources rupture through the Shumagin seismic gap that is believed to be a boundary for fault rupturing. The present study argues that when dealing with earthquake scenarios of very long return periods, such geologic boundaries could be potentially ruptured, as was the case with the 2007 Solomon Island earthquake that crossed a triple plate junction and the 2011 Tohoku earthquake that crossed multiple theoretical segment boundaries (Rong et al. 2014 and references therein). Also in the probabilistic tsunami hazard study of TPSWG (2006) for Seaside Oregon, and in Gonzalez et al. (2009), the Shumagin gap was over-lapped by a source positioned between the eastern Aleutians and Kodiak Island (Source 2 in Gonzalez et al. 2009).

3.2 Worst-case scenarios

Figure 6 shows the predicted run-up heights from all the proposed sources (Tables 3 and 4). It can be observed that the only sources that generate run-up heights greater than 10 m are the ones from Alaska (AA-1 and AA-2), resulting in maximum run-up values of 15.3 and 21.5 m, respectively. From the second methodology, source AA-5 and AA-6 produce the largest run-up values of 6.0 and 7.3 m, respectively, significantly lower than the AASZ sources designed using the maximum tsunami generation methodology. Based on the sensitivity analysis presented in the previous section and the predicted run-up, it is con-cluded that the AASZ poses the highest tsunami hazard to Central California than any other subduction zone, using both methodologies. Therefore, a more detailed analysis of the two proposed sources AA-1 and AA-2 is presented in this section since they can be considered as the worst-case scenarios for this particular location.

The maximum propagation tsunami amplitudes from scenarios AA-1 and AA-2 are shown in Fig. 7a, b, respectively. Both scenarios produce similar maximum amplitudes near the source region, while commensurate tsunami energy is beamed toward the study area from both sources. Figure 8a, b shows the predicted maximum free surface elevation (MFSE) for sources AA-1 and AA-2, respectively. Both scenarios produce similar MFSE patterns in the study area, with source AA-1 resulting into more consistent MFSE values in the range of 10–12 m, whereas source AA-2 produces higher MFSEs near the coast at latitudes below 35.2067°N. The variability of run-up along the coast from sources AA-1 and AA-2 can be observed in Fig. 6. For AA-1, the predicted average run-up is 10.0 m,
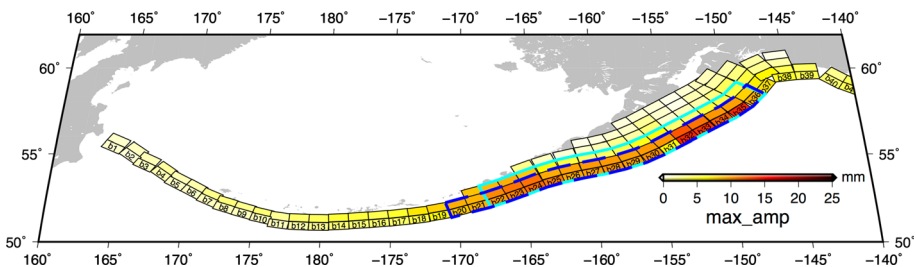

Fig. 5 NOAA's unit sources and numbering along the Alaska-Aleutians subduction zone. *Colors* represent the maximum amplitude at the numerical tide gauge offshore of Pismo Beach/southwest of Morro Bay, Central California, from each unit source using 1 m slip. The rupture areas of sources AA-1 and AA-2 are shown with the *cyan continuous line* and *dashed blue colors*, respectively
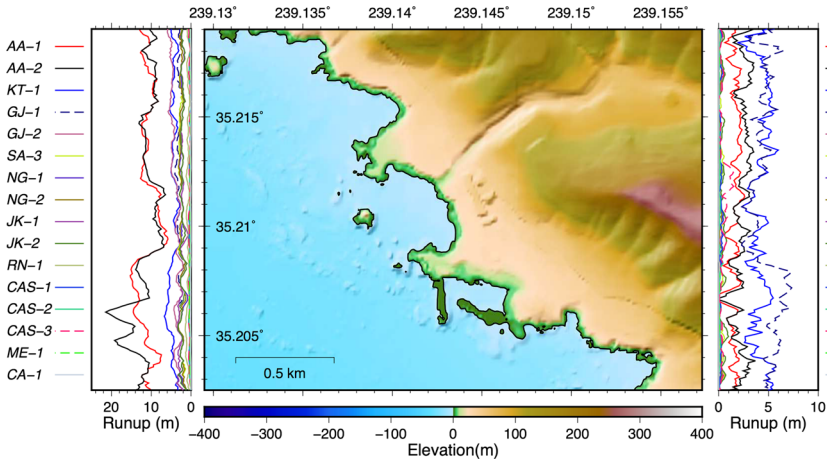
Fig. 6 Digital elevation model (DEM, referenced at MHW) of the study area (*middle*) and calculated run-up heights from all scenarios using the first and second methodologies (*left* and *right*, respectively). The run-up curves were filtered using a 5-point moving average scheme
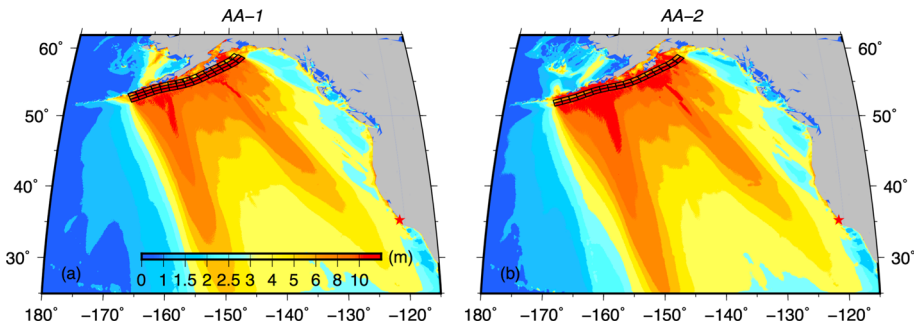

Fig. 7 a Maximum tsunami amplitude from scenarios AA-1 and **b** AA-2. The unit sources considered for the source are shown with the black rectangles. The study area is shown with the *red star*

with a standard deviation of 3.4 m and a maximum of 15.3 m. The predicted average run-up from AA-2 is 10.9 m with a standard deviation of 3.7 m. The predicted maximum is 21.5 m, which is about 30% higher than that from AA-1. The inundation area for both scenarios is not extensive due to the steep topography.

Minimum free surface elevations from both scenarios, relative to mean low water (MLW), are presented in Fig. 8c, d. Both scenarios predict minimum amplitudes ranging from 0 to −5 m along the coast. Finally, tsunami waves from both scenarios begin to affect the Central California coast after approximately 5 h of the events, with the largest wave occurring within the first hour and a half after the first wave arrives. Both events would provide enough time to take necessary emergency precautions for a timely evacuation.
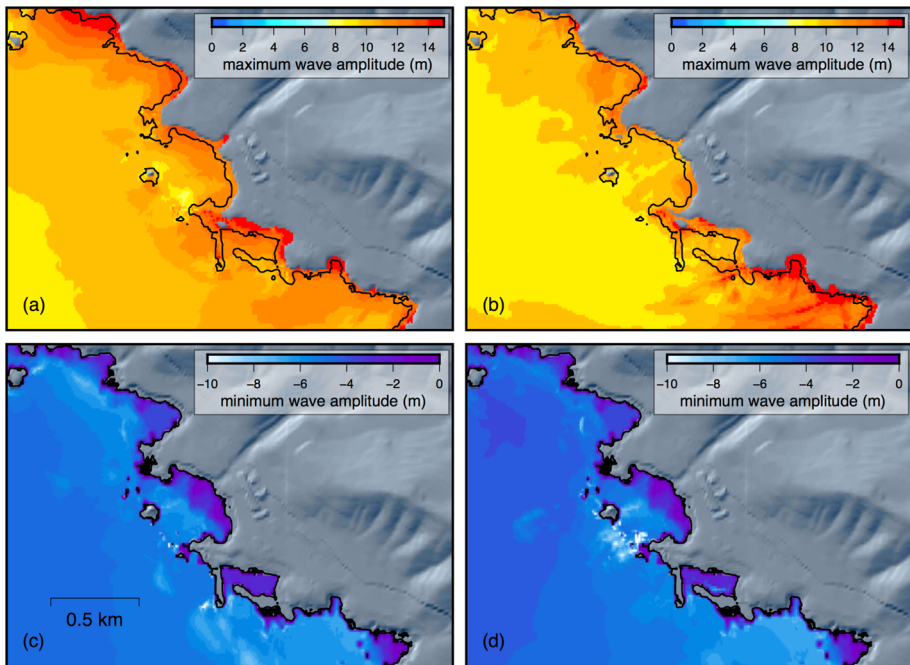
Fig. 8 **a** Maximum free surface elevations from scenario AA-1 and **b** AA-2 relative to mean high water (MHW). **c** Minimum free surface elevations from scenario AA-1 and **d** AA-2 relative to mean low level (MLW). The spatial extent of the plots is the same as in Fig. 6

4 Conclusions

This study presents two methodologies to determine PMT amplitudes for any coastal site in the Pacific. The preliminary sensitivity analysis, which utilizes the NOAA/PMEL unit source database, provides a strong indication on which subduction zones beam the most energy to a particular study area and can be implemented for any type of THA study.

The earthquake scenarios designed to determine the PMT are based on the maximum magnitudes assigned to major subduction zones by three recent studies: MC08, GEM15 and RO14. MC08 and GEM15 used a similar methodology to calculate the maximum magnitudes for each subduction zone. Both studies obtain the maximum magnitude earthquake by examining the geologic settings of each subduction zone. They discretized the word's subduction zones into different segments based on changes in plate pair convergence. Then the maximum available length to compute the maximum moment magnitude is identified. On the other hand, RO14 estimates the maximum earthquake magnitude as a function of return period using the *TGR* distribution. A return period of 10,000 years was selected in this study to compare with the MC08- and GEM15-suggested maximum magnitudes.

In absence of a definite argument for which approach is most appropriate, the maximum of all suggested magnitudes was selected as the representative worst-case scenario for each subduction zone. This simplification, which greatly affects the results of a THA study looking at very low probabilities of exceedance, can be revised as the subject of maximum

magnitude earthquakes matures. Moreover, the extreme slip values (>100 m) assigned to certain maximum magnitude scenarios do not necessarily adhere to current perception of fault rupturing. The extreme slip is a direct result of fitting a very large magnitude earthquake in a confined fault rupture area. In our analysis, we also suggested an alternative methodology to assign maximum magnitudes that are based on subduction-zone-specific scaling relations between magnitude and rupture area. The resulting maximum magnitudes are significantly lower, subsequently leading to less tsunami generation potential. This result is a testament to the diversity of results that can be obtained using different methodologies currently found in the literature and highlights the need to reach a consensus on what maximum magnitudes should be used for THAs in the return periods that apply to sensitive coastal infrastructure.

In the case study presented for Central California, only far-field source were considered, but the methodology can be extended to also include near-field events. For the near-field sources, the analysis should take into account the uncertainty in the rupture characteristics and fault geometry (e.g., through a Monte Carlo implementation), since they have a strong influence on run-up distribution near the fault rupture area.

References

Ayca A, Lynett P (2016) Effect of tides and source location on nearshore tsunami-induced currents. J Geophys Res-Oceans 121(12):8807–8820

Barberopoulou A, Borrero JC, Uslu B, Kalligeris N, Goltz JD, Synolakis CE, Wilson RI (2009) New maps of California to improve tsunami preparedness, invited feature article. EOS Trans AGU 90(16):137–138

Berryman K, Wallace L, Hayes G, Bird P, Wang K, Basili R, Lay T, Stein R, Sagiya T, Rubin C, Barrientos S, Kreemer C, Litchfield N, Stirling M, Gledhill K, Haller K, Costa C (2015) The GEM Faulted Earth Subduction Interface Characterization Project, Version 2.0, April 2015, GEM Faulted Earth Global Component. http://www.nexus.globalquakemodel.org/gem-faulted-earth/posts

Bilek SL, Lay T (1999) Rigidity variations with depth along interpolate megathrust faults in subduction zones. Nature 400:443–446

Bird, P (2003) An updated digital model of plate boundaries. Geochem Geophys 4(2)

Bird P, Kagan YY (2004) Plate-tectonic analysis of shallow seismicity: apparent boundary width, beta-value, corner magnitude, coupled lithosphere thickness, and coupling in seven tectonic settings. Bull Seismol Soc Am 94:2380–2399

Blaser L, Krüger F, Ohrnberger M, Scherbaum F (2010) Scaling relations of earthquake source parameter estimates with special focus on subduction environment. Bull Seismol Soc Am 100:2914–2926

Borrero JC, Dolan J, Synolakis CE (2001) Tsunami sources within the Eastern Santa Barbara Channel. Geophys Res Lett 28(4):643–647

Burwell D, Tolkova E, Chawla A (2007) Diffusion and dispersion characterization of a numerical tsunami model. Ocean Model 19:10–30

Chlieh M, Avouac JP, Hjorleifsdottir V, Song TA, Ji C, Sieh K, Sladen A, Hebert H, Prawirodirdjo L, Bock Y, Galetzka J (2007) Coseismic slip and afterslip of the great M_w 9.15 Sumatra-Andaman earthquake of 2004. Bull Seismol Soc Am 97(1A):S152–S173

Eisner RK, Borrero JC, Synolakis CE (2001) Inundation maps for the State of California In: ITS 2001 Proceedings, NTHMP Review Session, Paper R-4

Frankel AD, Petersen MD (2008) Cascadia Subduction Zone. U. S. Geol. Surv. Open File Rep. 2007-1437-L

Freymueller J, Beavan J (1999) Absence of strain accumulation in the western Shumagin segment of the Alaska subduction zone. Geophys Res Lett 26:3233–3236

Friday DZ, Taylor LA, Eakins BW, Carignan KS, Grothe PR, Lim E, Love MR (2011) Digital Elevation Models of Port San Luis, California: Procedures, Data Sources and Analysis, NOAA National Geophysical Data Center technical report, Boulder, CO

Fuchs Sir V (1982) Of ice and men: The story of the British Antarctic Survey, 1943-73. Anthony Nelson, Oswestry, p 383

Geist EL, Parsons T (2014) Undersampling power-law size distributions: effect on the assessment of extreme natural hazards. Nat Hazards 72:565–595

Geller RJ (2011) Shake-up time for Japanese seismology. Nature 472:407–409

Gica E, Spillane MC, Titov VV, Chamberlin CD, Newman JC (2008) Development of the forecast propagation database for NOAA's short-term inundation forecast for tsunamis (SIFT). NOAA OAR Technical Memorandum, OAR PMEL-139

Goldfinger C, Nelson CH, Morey AE, Johnson JE, Patton JR, Karabanov E, Gutierrez-Pastor J, Eriksson AT, Gracia E, Dunhill G, Enkin RJ, Dallimore A, Vallier T (2012) Turbidite event history: Methods and implications for Holocene paleoseismicity of the Cascadia subduction zone, U.S. Geol. Surv. Profess. Pap. 1661-F

Gonzalez FI, Geist EL, Jaffe B, Kanoglu U, Mofjeld H, Synolakis CE, Titov VV, Arcas D, Bellomo D, Carlton D et al (2009) Probabilistic tsunami hazard assessment at Seaside, Oregon, for near- and far-field seismic sources. J Geophys Res 114:C11023

Grantz A, Plafker G, Kachadoorian R (1964) Alska's good Friday earthquake, March 27, 1964: a preliminary geologic evaluation, U.S. Geological Survey report

Hanks TC, Kanamori H (1979) A moment magnitude scale. J Geophys Res 84:2348–2350

Houston JR, Garcia AW (1978) Type 16 flood insurance study: Tsunami predictions for the west coast of the continental United States. U.S. army engineer waterways experiment station technical report H-78-26

Johnson JM, Satake K (1997) Estimation of seismic moment and slip distribution of the April 1, 1946, Aleutian tsunami earthquake. J Geophys Res 102:11765–11774

Johnson JM, Tanioka Y, Ruff LJ, Sataki K, Kanamori H, Sykes LR (1994) The 1957 great Aleutian earthquake. Pure appl Geophys 142:3–28

Kagan YY (2002) Seismic moment distribution revisited: I. Statistical results. Geophys J Int 148:520–541

Kagan YY, Jackson DD (2013) Tohoku earthquake: a surprise? Bull Seismol Soc Am 103:1181–1194

Kanamori H (1970) The Alaska earthquake of 1964: radiation of long-period surface waves and source mechanism. J Geophys Res 75:901–925

Kanamori H (1972) Mechanism of tsunami earthquakes. Phys Earth Planet Inter 6(5):346–359

Kirby S, Geist E, Lee W, Scholl D, Blakely R (2005) Tsunami Source Characterization for Western Pacific Subduction Zones, A Preliminary Report. USGS1 Tsunami Subduction Source Working Group

Lander JF (1996) Tsunamis affecting Alaska 1737-1996. No. 31 in NGDC Key to Geophysical Research Documentation, National Geophysical Data Center, Boulder, CO

Lander JF, Lockridge PA, Kozuch MJ (1993) Tsunamis affecting the west coast of the United State 1806-1992, No. 29 in NGDC Key to Geophysical Research Documentation, National Geophysical Data Center, Boulder, CO

Liu-Zeng J, Heaton T, DiCaprio C (2005) The effect of slip variability on earthquake slip-length scaling. Geophys J Int 162:841–849

Loomis HG (1976) Tsunami wave runup heights in Hawaii. University of Hawaii, Honolulu, Hawaii Institute of Geophysics

López AM, Okal EA (2006) A seismological reassessment of the source of the 1946 Aleutian "tsunami" earthquake. Geophys J Int 165:835–849

Lynett PJ, Borrero J, Son S, Wilson R, Miller K (2014) Assessment of the tsunami-induced current hazard. Geophys Res Lett 41:2048–2055

McCaffrey R (1992) Oblique plate convergence, slip vectors, and forearc deformation. J Geophys Res 97:8905–8915

McCaffrey R (2008) Global frequency of magnitude 9 earthquakes. Geology 36(3):263–266

Murotani S, Satake K, Fujii Y (2013) Scaling relations of seismic moment, rupture area, average slip, and asperity size for M ∼ 9 subduction-zone earthquakes. Geophys Res Lett 40:5070–5074

Okada Y (1985) Surface deformation due to shear and tensile faults in a half-space. Bull Seism Soc Am 75(4):1135–1154

Okal EA (2015) The quest for wisdom: lessons from 17 tsunamis, 2004-2014. Philos Trans R Soc A 373:2053

Okal EA, Hébert H (2007) Far-field simulation of the 1946 Aleutian tsunami. Geophys J Int 169:1229–1238

Okal EA, Synolakis CE (2004) Source discriminants for near-field tsunamis. Geophys J Int 158:899–912

Okal EA, Synolakis CE (2008) Far-field tsunami hazard from mega-thrust earthquakes in the Indian Ocean. Geophys J Int 172:995–1015

Okal EA, Plafker G, Synolakis CE, Borrero JC (2003) Near-Field survey of the 1946 Aleutian Tsunami of Unimak and Sanak Islands. Bull Seism Soc Am 93(3):1226–1234

Percival DB, Arcas D, Denbo DW, Eble MC, Gica E, Mofjeld HO, Spillane MC, Tang L, Titov VV (2009) Extracting tsunami source parameters via inversion of DART buoy data. NOAA Tech. Memo. OAR PMEL-144

Plafker G (1969) Tectonics of the March 27, 1964 Alaska earthquake, U.S. Geol. Surv. Prof. Paper 543-I

Plafker G (1972) Alaskan earthquake of 1964 and Chilean earthquake of 1960: implications for arc tectonics. J Geophys Res 77:901–925

Rong Y, Jackson DD, Magistrale H, Goldfinger C (2014) Magnitude limits of subduction zone earthquakes. Bull Seism Soc Am 104(5):2359–2377

Shao G, Li X, Ji C, Maeda T (2011) Focal mechanism and slip history of the 2011 M_w 9.1 off the Pacific coast of Tohoku Earthquake, constrained with tele seismic body and surface waves. Earth Planets Earth 63:559–564

Spaeth MG, Berkman SC (1965) The Tsunami of March 38, 1964 as Recorded at Tide Stations. U.S. Coast and Geod, Survey, p 59

Strasser FO, Arango MC, Bommer JJ (2010) Scaling of the source dimensions of interface and intraslab subduction-zone earthquakes with moment magnitude. Seismol Res Lett 81:941–950

Suleimani E, Nicolsky D, Haeussler PJ, Hansen R (2011) Combined effects of tectonics and landslide-generated tsunami runup at Seaward, Alaska during the Mw 9.2 1964 earthquake. Pure appl Geophys 168(6):1053–1074

Synolakis CE, Kanoglu U (2015) The Fukushima accident was preventable. Philos Trans R Soc A 373:2053

Synolakis CE, McCarthy D, Titov, VV, Borrero JC editors (1997) Evaluating the Tsunami Risk in California, California and the World Ocean 97 Proceeding of the Conference, San Diego, California. ASCE

Synolakis CE, Bardet JP, Borrero J, Davies H, Okal E, Silver E, Sweet J, Tappin D (2002) Slump origin of the 1998 Papua New Guinea tsunami. Philos Trans R Soc Ser A 458:763–789

Synolakis CE, Bernard EN, Titov VV, Kanoglu U, Gonzalez FI (2008) Validation and verification of tsunami numerical models. Pure appl Geophys 165:2197–2228

Tang L, Titov VV, Chamberlin CD (2009) Development, testing, and applications of site-specific tsunami inundation models for real-time forecasting. J Geophys Res 114(C12025)

Tang L, Titov VV, Chamberlin CD (2010) A Tsunami Forecast Model for Hilo, Hawaii. NOAA OAR Special Report, PMEL Tsunami Forecast Series, vol. 1

Taylor FW, Briggs RW, Frohlich C, Brown A, Hornbach M, Papabatu AK, Meltzner AJ, Billy B (2008) Rupture across arc segment and plate boundaries in the 1 April 2007 Solomons earthquake. Nat Geosci 1:253–257

Titov VV (2009) Tsunami forecasting. Chapter 12 in The Sea, Volume 15: Tsunamis. Harvard University Press, Cambridge, pp 371–400

Titov V, González FI (1997) Implementation and testing of the Method of Splitting Tsunami (MOST) model. NOAA Tech. Memo. ERL PMEL-112 (PB98-122773), NOAA/Pacific Marine Environmental Laboratory, Seattle, WA

Titov VV, Synolakis CE (1995) Modeling of breaking and nonbreaking long wave evolution and runup using VTSC-2. J Waterw Port Coast Ocean Eng 121:308–316

Titov VV, Synolakis CE (1998) Numerical modeling of tidal wave runup. J Waterw Port Coast Ocean Eng 124:157–171

Titov VV, Mofjeld HO, González FI, Newman JC (1999) Offshore forecasting of Hawaiian tsunamis generated in Alaskan-Aleutian subduction zone: Pacific Marine Environmental Laboratory (PMEL), PMEL-114

Titov VV, Moore CW, Greenslade DJM, Pattiaratchi C, Badal R, Synolakis CE, Kanoglu U (2011) A new tool for inundation modeling; community modeling interface for tsunamis (ComMIT). Pure appl Geophys 168:2121–2131

Tsunami Pilot Study Working Group (TPSWG) (2006) Seaside, Oregon Tsunami Pilot Study-Modernization of FEMA Flood Hazard Maps, NOAA OAR Special Rep., NOAA/OAR/PMEL, Seattle, WA, 94 pp. +7 appendices

USC Tsunami Research Center website: http://www.usc.edu/dept/tsunamis/alaska/. Accessed 7/9/2015

Uslu B (2008) Deterministic and probabilistic tsunami studies in California from near and farfield sources, PhD thesis, University of Southern California

Wei Y, Chamberlin C, Titov VV, Tang L, Bernard EN (2012) Modeling of 2011 Japan Tsunami—lessons for near-field forecast. Pure Appl Geophys 170(1309):1331

Wells DL, Coppersmith KJ (1994) New empirical relationships among magnitude, rupture length, rupture width, rupture area and surface displacement. Bull Seism Soc Am 84:974–1002

Wesson RL, Frankel AD, Mueller CS, Harmsen SC (1999) Probabilistic Seismic Hazard Maps of Alaska. U.S. Geological Survey, Open-File Report 99-36

Wesson RL, Boyd OS, Mueller CS, Bufe CG, Frankel AD, Petersen MD (2007) Revision of Time-Independent Probabilistic Seismic Hazard Maps for Alaska, USGS Open-File Report 2007-1043

Wilson BW, Torum A (1968) Runup heights of the major tsunami on north American coasts, in: The Great Alaska Earthquake of 1964, National Research Council (U.S.), Committee on the Alaska Earthquake, National Academies